Supplemental Material
Non-uniform electro-osmotic flow drives fluid−structure instability

Evgeniy Boyko[§,1] Ran Eshel[§,1] Amir D. Gat,[1] and Moran Bercovici[1,2,*]

[1] *Faculty of Mechanical Engineering, Technion − Israel Institute of Technology, Haifa, 3200003 Israel*
[2] *Department of Mechanical Engineering, The University of Texas at Austin, Austin, Texas 78712, USA*
[§] *Equal contribution*

CONTENTS

S.1. DETAILS OF EXPERIMENTAL SETUP

S.1.1. Fabrication

As illustrated in Fig. S1, the elastic sheet and the microfluidic chamber which supports it are one structural unit which is made in a single molding process of polydimethylsiloxane (PDMS) (1:10 crosslinker to resin ratio, 184 Silicone Elastomer, Sylgard, USA). The mold consists of a 30×15 mm layer of 104 μm thick Kepton tape (Dupont, USA) placed at the center of an otherwise smooth silicon wafer. On top of this mold we poured 5 gr of pre-mixed PDMS and spun it for 30 s at 150 rpm, followed by 40 s at 420 rpm, resulting in a final thickness of 142 μm in the smooth regions of the wafer (which will serve as the boundaries of the chamber), and 38 μm above the Kepton (which will serve as the thin elastic membrane). We baked the PDMS at 180 C for 2 hours, and then peeled off the mold and exposed it to plasma using a corona discharge wand (BD-20V, Electro-Technic Products, USA). Next, we attached the plasma-exposed side to a rigid acrylic plate containing a 15×15 mm square opening at its center and two 4 mm through-holes located on either side of the opening at a distance of 25 mm from one another, which are to serve as reservoirs. Through these holes, we then also punched the PDMS layer using a 4 mm diameter biopsy punch.

The floor of the chamber was made of a standard glass slide. We covered half of the slide with Kepton tape, and functionalize the exposed part with poly(allylamine hydrochloride) (PAH) by pipetting on top of it 100 μL of 0.05% solution of PAH (Sigma Aldrich, USA) in water, incubating for 5 min, and rinsing with DI water. We attached the functionalized slide to the chamber using UV adhesive (NOA68, Norland, USA) which we applied uniformly to the edges of the PDMS chamber using a spatula, and then exposed it to UV for 15 min.

On top of the exposed elastic membrane we placed our rigid plate − a 10×10 mm piece of acrylic, coated with fluorescent micro-beads (Fluoro-Max red fluorescent polymer microspheres, 2 μm diameter, Thermo Fisher Scientific, USA). To coat the plate, we pipetted onto its surface 15 μL of a water solution containing 5×10^{-4}% solids, and

allowed the liquid to evaporate.

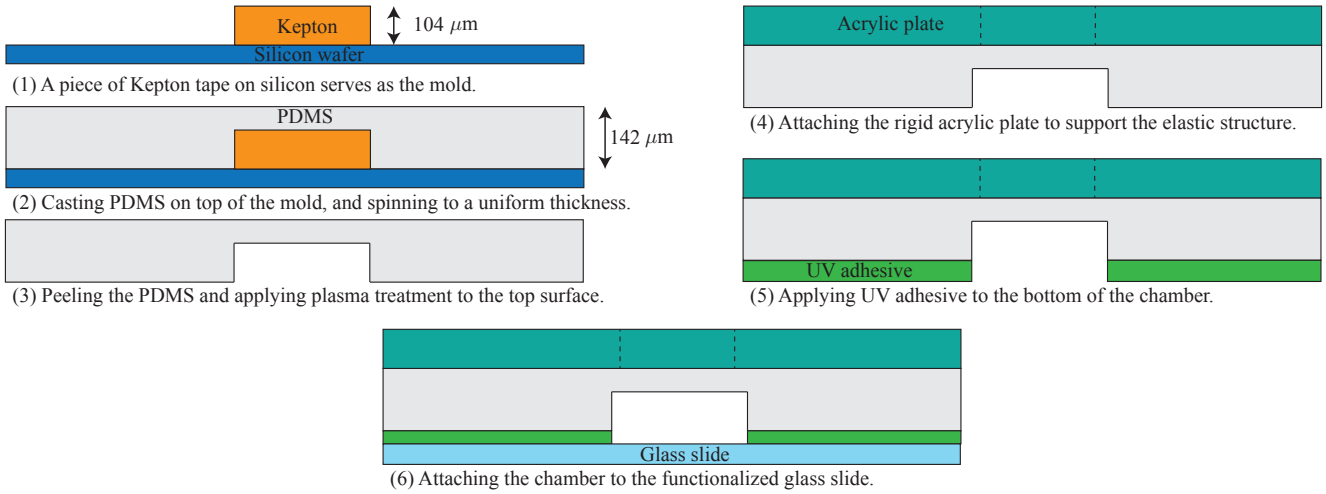

FIG. S1. Schematic illustration of the experimental system fabrication process. (1) We created the mold by attaching a Kepton tape to the smooth silicon surface. (2) We casted the PDMS on top of the Kepton mold and spun it to a uniform thickness. (3) We peeled the PDMS and treated the top of the chamber with plasma. (4) We attached it to an acrylic plate for mechanical rigidity. (5) We applied UV adhesive uniformly on the bottom of the chamber. (6) We attached the bottom of the chamber to the functionalized glass surface, and cured the adhesive using a UV lamp for 15 min.

S.1.2. Optical system

We imaged the beads using an upright microscope (AZ-100, Nikon, Japan) equipped with an LED light source (Sola SE, Lumencore, USA) and a TRITC filter cube (Nikon G-2E/C, 540/25 nm excitation, 605/55 nm Emission, and 565 nm dichroic mirror). We used a 5× 0.5 NA objective with additional internal magnification of 5×, leading to total magnification of 25×. In addition, in order to modify the point spread function (PSF) of the optical system, we placed a cylindrical lens (focal length $f = 150$ mm, LK4432RM, Thorlabs, USA) 5 mm in front of the camera image plane [1]. We captured image sequences at a frame rate of 2 fps and an exposure time of 100 ms using an sCMOS camera (Andor Zyla 4.2, Oxford Instruments, UK) operated by NIS elements software (v. 5.02, Nikon, Japan).

S.1.3. Calibration of vertical translation measurements

Prior to the measurement, we created a calibration library consisting of images of a single bead at different (known) vertical positions relative to a fixed focal point of the optics. The vertical positions were controlled using a piezo stage (NanoscanZ 200, Prior Scientific, USA) at intervals of 0.5 μm. As shown in Fig. 1(c) of the main text, the use of a cylindrical lens in the optical train results in distinct shapes of the PSF for different vertical positions. In subsequent experimental measurements, the vertical position of the plate was determined by cross-correlating images of individual beads with this calibration library, and choosing the one which provides the highest correlation. This process is repeated for multiple beads available at the field of view, and the final reported location is the average of these values. Figure S2 presents a test case where the optically measured vertical location is plotted against the controlled (known position), showing very good agreement over a span of approximately 140 μm, which covers well the range of motion in our experiments.

S.1.4. Additional experimental data

Figure 2 in the main text presents one set of experiments, showing the dynamics of the deformation for different electric fields. Figure S3 presents again this set of experiments (Fig. S3(d)), as well as 3 additional independent sets of experiments (Figs. S3(a–c)). In all cases we observed the distinct dynamic behavior described in the paper –

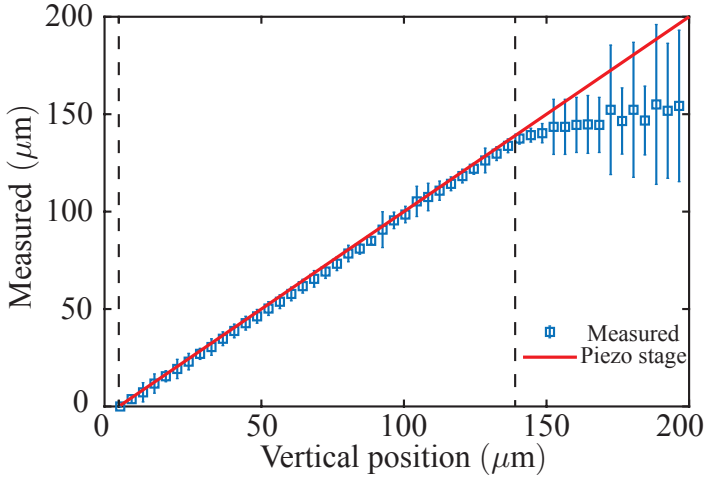

FIG. S2. Comparison of the optically measured vertical position of the plate with its controlled position as set by the piezo stage. The blue squares indicate the mean measured position based on 4 imaged beads, with a 95% confidence bars. The red line shows the known value, based on the controlled position of the piezo stage. The vertical dashed black lines mark the range we used in subsequent measurements.

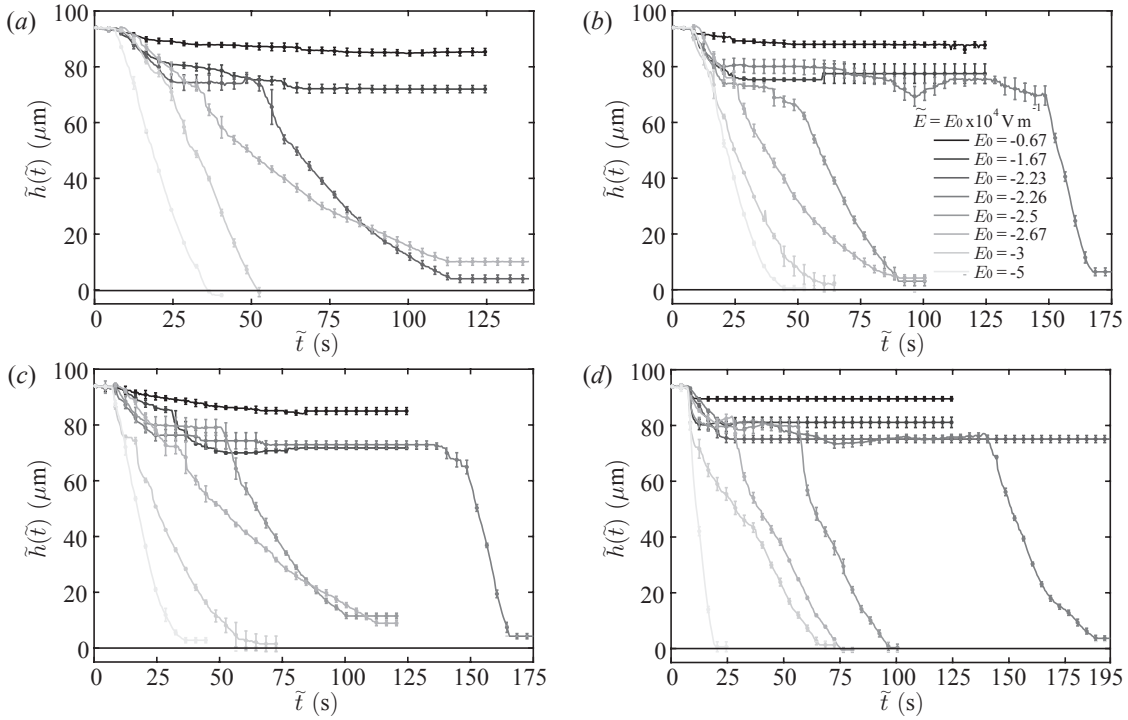

FIG. S3. Experimental results, showing the evolution of the fluidic gap in time in several independent experiments. (a–c) We initially performed all experiments at electric fields of $-0.67, -1.67, -2.5, -2.67, -3$, and -5×10^4 V/m on the same experimental setup. (d) We then constructed a new experimental setup and added two additional electric fields (-2.23 and -2.26×10^4 V/m) in order to capture as accurately as possible the threshold field for the transition to instability.

stability up to a threshold electric field value and a bottleneck instability for a sufficiently large field, which shorten in time as the field is further increased.

S.2. DERIVATION OF GOVERNING EQUATIONS FOR THE ONE-DIMENSIONAL MODEL

We here detail the derivation of the one-dimensional model governing the gap $\tilde{h}(\tilde{t})$ between the two plates. We consider a viscous liquid film confined between a rigid surface and a rigid body of mass $\tilde{m}$ and length $\tilde{l}_m$. The rigid body is placed on the top of a pre-stretched elastic sheet of length $\tilde{l}_{sheet}$, which we model as a linear spring with stiffness $\tilde{k}$, as shown in Fig. S4 and Fig. 1(d) of the main text. The liquid film is connected to two fluidic reservoirs of length $\tilde{l}_{res}$ at a distance $\tilde{L}$ from one another, through which the electric field is activated either by applying a constant voltage $\tilde{V}$ or a constant current $\tilde{I}$. We employ a Cartesian coordinate system $(\tilde{x}, \tilde{z})$, whose $\tilde{x}$ axis lies at the lower flat surface and $\tilde{z}$ is perpendicular thereto. As in our experimental setup, we assume that a non-uniform electro-osmotic slip velocity $\tilde{u}_{\mathrm{EOF}}(\tilde{x})$ on the bottom rigid surface drives the fluid from the center to the edges of the chamber resulting in a negative gauge pressure field, which in turn leads to change the gap $\tilde{h}(\tilde{t})$. Due to conservation of mass, the heights of the fluid columns in the left and right reservoirs, $\tilde{h}_L(\tilde{t})$ and $\tilde{h}_R(\tilde{t})$, are also time-varying.

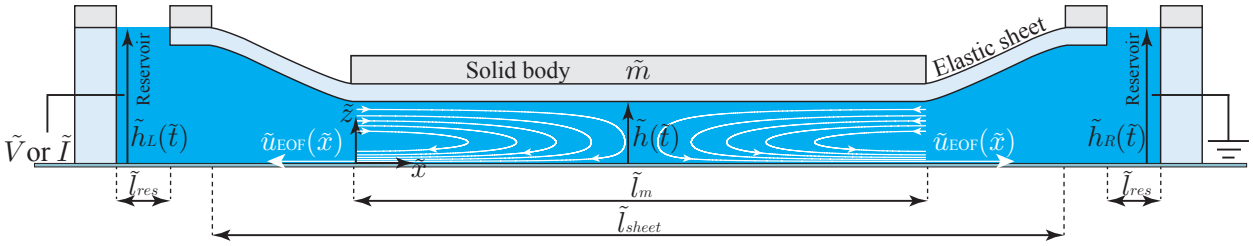

FIG. S4. Schematic side view of the modeled configuration, showing the relevant physical and geometric parameters.

S.2.1. Governing equations in dimensional form

Considering a shallow fluidic layer and negligible fluidic inertia, represented by small Womersley and reduced Reynolds numbers,

$$\epsilon = \frac{\tilde{h}_0}{\tilde{l}_m} \ll 1, \quad Wo = \frac{\tilde{\rho}\tilde{h}_0^2}{\tilde{\mu}\tilde{t}^*} \ll 1, \quad \epsilon Re = \epsilon\frac{\tilde{\rho}\tilde{u}^*\tilde{h}_0}{\tilde{\mu}} \ll 1, \tag{S1}$$

the fluid motion between the plates is governed by the lubrication equations [2],

$$\frac{\partial\tilde{u}}{\partial\tilde{x}} + \frac{\partial\tilde{w}}{\partial\tilde{z}} = 0, \quad \frac{\partial\tilde{p}}{\partial\tilde{x}} = \tilde{\mu}\frac{\partial^2\tilde{u}}{\partial\tilde{z}^2}, \quad \frac{\partial\tilde{p}}{\partial\tilde{z}} = -\tilde{\rho}\tilde{g}, \tag{S2}$$

where $\tilde{u}^*$ is the characteristic velocity in the $\hat{\boldsymbol{x}}$ direction, $\tilde{t}^*$ is the characteristic time scale and $\tilde{g}$ is the acceleration of gravity. The lubrication equations (S2) are subject to an EOF slip velocity and no-penetration at the bottom surface, as well as no-slip and a kinematic boundary condition at the top plate,

$$(\tilde{u}, \tilde{w})\,|_{\tilde{z}=0} = \left(\tilde{u}_{\mathrm{EOF}}(\tilde{x}, \tilde{t}), 0\right), \quad (\tilde{u}, \tilde{w})\,|_{\tilde{z}=\tilde{h}} = \left(0, \frac{\mathrm{d}\tilde{h}(\tilde{t})}{\mathrm{d}\tilde{t}}\right). \tag{S3}$$

The electro-osmotic slip velocity $\tilde{u}_{\mathrm{EOF}}(\tilde{x}, \tilde{t})$ is given by the Helmholtz–Smoluchowski equation [3],

$$\tilde{u}_{\mathrm{EOF}}(\tilde{x}, \tilde{t}) = -\frac{\tilde{\varepsilon}\tilde{\zeta}(\tilde{x})}{\tilde{\mu}}\tilde{E}(\tilde{t}), \tag{S4}$$

where $\tilde{\varepsilon}$ is the fluid permittivity, $\tilde{\zeta}(\tilde{x})$ is the zeta potential and $\tilde{E}(\tilde{t})$ is the imposed electric field.

In microfluidic devices, the electric field $\tilde{E}$ is commonly created either by applying a constant voltage or a constant electric current. For the case of a constant applied voltage drop $\tilde{V}$ over the distance $\tilde{L}$, the resulting electric field is constant and uniform

$$\tilde{E} = \frac{\tilde{V}}{\tilde{L}}, \tag{S5}$$

while for the case of a constant applied current $\tilde{I}$, current conservation dictates that the resulting electric field is time-varying according to

$$\tilde{E}(t) = \frac{\tilde{I}}{\tilde{\sigma}\tilde{w}_m}\frac{1}{\tilde{h}(\tilde{t})}, \tag{S6}$$

where $\tilde{\sigma}$ [$\mathrm{S\,m^{-1}}$] is the fluid conductivity and $\tilde{w}_m\tilde{h}(\tilde{t})$ is the cross-section area of the channel. In order to compare between these two actuation modes, we assume that at time $\tilde{t}=0$ both modes produce the same electric field $\tilde{E}$, i.e. that $\tilde{I}/\tilde{\sigma}\tilde{w}_m = \tilde{E}\tilde{h}_0$ and thus

$$\tilde{E}(\tilde{t}) = \frac{\tilde{I}}{\tilde{\sigma}\tilde{w}_m}\frac{1}{\tilde{h}(\tilde{t})} = \tilde{E}\frac{\tilde{h}_0}{\tilde{h}(\tilde{t})}. \tag{S7}$$

Substituting Eqs. (S5) and (S7) into Eq. (S4), we obtain explicit expressions for the electro-osmotic slip velocity for both actuation modes

$$\tilde{u}_{\mathrm{EOF}}(\tilde{x},\tilde{t}) = \begin{cases} -\dfrac{\tilde{\varepsilon}\tilde{\zeta}(\tilde{x})\tilde{E}}{\tilde{\mu}} & \text{Constant applied voltage} \\ -\dfrac{\tilde{\varepsilon}\tilde{\zeta}(\tilde{x})\tilde{E}}{\tilde{\mu}}\dfrac{\tilde{h}_0}{\tilde{h}(\tilde{t})} & \text{Constant applied currect} \end{cases}. \tag{S8}$$

Integrating the momentum equation in the $\hat{\boldsymbol{x}}$ direction, Eq. (S2), twice with respect to $\tilde{z}$ and applying the boundary conditions, Eq. (S3) yields

$$\tilde{u}(\tilde{x},\tilde{z},\tilde{t}) = \frac{1}{2\tilde{\mu}}\frac{\partial\tilde{p}}{\partial\tilde{x}}\tilde{z}(\tilde{z}-\tilde{h}) + \tilde{u}_{\mathrm{EOF}}(\tilde{x})\left(1-\frac{\tilde{z}}{\tilde{h}}\right). \tag{S9}$$

The corresponding one-dimensional continuity equation reads

$$\frac{\mathrm{d}\tilde{h}(\tilde{t})}{\mathrm{d}\tilde{t}} + \frac{\partial\tilde{Q}}{\partial\tilde{x}} = 0, \tag{S10}$$

where $\tilde{Q}$ is the volume flux, obtained from Eq. (S9) as

$$\tilde{Q}(\tilde{x},\tilde{t}) = \int_0^{\tilde{h}}\tilde{u}d\tilde{z} = -\frac{\tilde{h}(\tilde{t})^3}{12\tilde{\mu}}\frac{\partial\tilde{p}}{\partial\tilde{x}} + \frac{1}{2}\tilde{h}(\tilde{t})\tilde{u}_{\mathrm{EOF}}(\tilde{x},\tilde{t}). \tag{S11}$$

Substituting Eq. (S11) into Eq. (S10), we obtain the governing equation for the gap between the two surfaces $\tilde{h}(\tilde{t})$,

$$\frac{\mathrm{d}\tilde{h}(\tilde{t})}{\mathrm{d}\tilde{t}} - \frac{\tilde{h}(\tilde{t})^3}{12\tilde{\mu}}\frac{\partial^2\tilde{p}(\tilde{x},\tilde{z},\tilde{t})}{\partial\tilde{x}^2} + \frac{1}{2}\tilde{h}(\tilde{t})\frac{\partial\tilde{u}_{\mathrm{EOF}}(\tilde{x},\tilde{t})}{\partial\tilde{x}} = 0. \tag{S12}$$

Integrating the momentum equation in the $\hat{\boldsymbol{z}}$ direction, Eq. (S2), the fluidic pressure $\tilde{p}(\tilde{x},\tilde{z},\tilde{t})$ is given by

$$\tilde{p}(\tilde{x},\tilde{z},\tilde{t}) = \tilde{p}_0(\tilde{x},\tilde{t}) - \tilde{\rho}\tilde{g}\tilde{z}, \tag{S13}$$

where the second term on the right-hand side represents the hydrostatic contribution to the pressure, and the first term represents all other contributions.

We consider the following boundary conditions for the pressure at the edges of the rigid plate

$$\tilde{p}(\tilde{x}=0,\tilde{z}=\tilde{h}_L,\tilde{t}) = \tilde{p}_0(\tilde{x}=0,\tilde{t}) - \tilde{\rho}\tilde{g}\tilde{h}_L(\tilde{t}) = 0 \quad \text{and} \quad \tilde{p}(\tilde{x}=\tilde{l}_m,\tilde{z}=\tilde{h}_R,\tilde{t}) = \tilde{p}_0(\tilde{x}=\tilde{l}_m,\tilde{t}) - \tilde{\rho}\tilde{g}\tilde{h}_R(\tilde{t}) = 0, \tag{S14}$$

corresponding to a hydrostatic pressure distribution with a zero gauge value in the reservoirs at $\tilde{z}=\tilde{h}_L(\tilde{t})$ (left reservoir) and $\tilde{z}=\tilde{h}_R(\tilde{t})$ (right reservoir), respectively.

We note that while there is an additional pressure drop between the reservoirs and the edges of the rigid plate due to viscous resistance, this additional resistance does not change the form of the final governing equation (Eq. (S27) derived below), and only affects the values of its coefficients. For simplicity and clarity we therefore do not account for this pressure drop in the boundary conditions (S14).

Solving Eq. (S12) using Eqs. (S13) and (S14), we obtain the expression for the pressure $\tilde{p}(\tilde{x},\tilde{z},\tilde{t})$

$$\tilde{p}(\tilde{x},\tilde{z},\tilde{t}) = \frac{6\tilde{\mu}}{\tilde{h}^3}\frac{\mathrm{d}\tilde{h}(\tilde{t})}{\mathrm{d}\tilde{t}}\tilde{x}(\tilde{x}-\tilde{l}_m) + \frac{6\tilde{\mu}}{\tilde{h}^2}\left[\tilde{A}(\tilde{x},\tilde{t}) - \frac{\tilde{x}}{\tilde{l}_m}\tilde{A}(\tilde{l}_m,\tilde{t})\right] + \tilde{\rho}\tilde{g}\left[\tilde{h}_L(\tilde{t}) - \tilde{z} + \frac{\tilde{x}}{\tilde{l}_m}(\tilde{h}_R(\tilde{t}) - \tilde{h}_L(\tilde{t}))\right], \tag{S15}$$

where $\tilde{A}(\tilde{x},\tilde{t})$ is defined as

$$\tilde{A}(\tilde{x},\tilde{t}) = \int_0^{\tilde{x}} \tilde{u}_{\mathrm{EOF}}(\tilde{x},\tilde{t})\mathrm{d}\tilde{x}. \tag{S16}$$

Substituting $\tilde{z} = \tilde{h}$ into Eq. (S15) and integrating the result with respect to $\tilde{x}$ from 0 to $\tilde{l}_m$, provides the force $\tilde{F}_p$ (per unit width) that the fluid pressure exerts on the rigid body

$$\tilde{F}_p(\tilde{t}) = -\frac{\tilde{\mu}\tilde{l}_m^3}{\tilde{h}(\tilde{t})^3}\frac{\mathrm{d}\tilde{h}(\tilde{t})}{\mathrm{d}\tilde{t}} + \frac{6\tilde{\mu}\tilde{B}}{\tilde{h}(\tilde{t})^2} + \tilde{\rho}\tilde{g}\tilde{l}_m\left[\frac{1}{2}(\tilde{h}_L(\tilde{t}) + \tilde{h}_R(\tilde{t})) - \tilde{h}(\tilde{t})\right], \tag{S17}$$

where $\tilde{B}$ is defined as

$$\tilde{B} = \int_0^{\tilde{l}_m} \tilde{A}(\tilde{x},\tilde{t})\mathrm{d}\tilde{x} - \frac{\tilde{A}(\tilde{l}_m,\tilde{t})\tilde{l}_m}{2} = -\frac{\tilde{\varepsilon}\tilde{E}(\tilde{t})}{\tilde{\mu}}\left[\int_0^{\tilde{l}_m}\left[\int_0^{\tilde{x}}\tilde{\zeta}(\tilde{\xi})\mathrm{d}\tilde{\xi}\right]\mathrm{d}\tilde{x} - \frac{\tilde{l}_m}{2}\int_0^{\tilde{l}_m}\tilde{\zeta}(\tilde{\xi})\mathrm{d}\tilde{\xi}\right]. \tag{S18}$$

Assuming that the initial volume of the fluid is conserved implies that $\tilde{h}(\tilde{t})$, $\tilde{h}_L(\tilde{t})$ and $\tilde{h}_R(\tilde{t})$ are related through

$$\tilde{h}_i(2\tilde{l}_{res} + \tilde{l}_{sheet}) = (\tilde{h}_L(\tilde{t}) + \tilde{h}_R(\tilde{t}))\tilde{l}_{res} + \frac{1}{2}(\tilde{h}(\tilde{t}) + \tilde{h}_i)(\tilde{l}_{sheet} - \tilde{l}_m) + \tilde{h}(\tilde{t})\tilde{l}_m \tag{S19}$$

which after some rearrangement yields

$$\frac{1}{2}(\tilde{h}_L(\tilde{t}) + \tilde{h}_R(\tilde{t})) - \tilde{h}(\tilde{t}) = \left[1 + \frac{\tilde{l}_m + \tilde{l}_{sheet}}{4\tilde{l}_{res}}\right](\tilde{h}_i - \tilde{h}(\tilde{t})). \tag{S20}$$

Substituting Eq. (S20) into Eq. (S17), we eliminate the dependence of $\tilde{F}_p$ on $\tilde{h}_L(\tilde{t})$ and $\tilde{h}_R(\tilde{t})$, and express the force solely in terms of $\tilde{h}(\tilde{t})$

$$\tilde{F}_p(\tilde{t}) = -\frac{\tilde{\mu}\tilde{l}_m^3}{\tilde{h}(\tilde{t})^3}\frac{\mathrm{d}\tilde{h}(\tilde{t})}{\mathrm{d}\tilde{t}} + \frac{6\tilde{\mu}\tilde{B}}{\tilde{h}(\tilde{t})^2} + \left[1 + \frac{\tilde{l}_m + \tilde{l}_{sheet}}{4\tilde{l}_{res}}\right]\tilde{\rho}\tilde{g}\tilde{l}_m(\tilde{h}_i - \tilde{h}(\tilde{t})). \tag{S21}$$

The first term on the right-hand side of Eq. (S21) represents the viscous resistance, the second term represents the electro-osmotic force which can be either attractive or repulsive depending on the sign of $\tilde{B}$, and the last term represents the restoring effect of the hydrostatic pressure.

Additional electric force, which acts on the plate apart from the electro-osmotic force, is the dielectric force arising from the Maxwell stresses. Since the liquid permittivity is much greater than the permittivity of PDMS and air, we may neglect the contribution to the Maxwell stress from the PDMS side of the interface. Based on these assumptions, the resulting dielectric force pushes upwards the rigid body and is given by [4]

$$\tilde{F}_d(\tilde{t}) = \frac{1}{2}\tilde{\varepsilon}\tilde{E}(\tilde{t})^2\tilde{l}_m. \tag{S22}$$

Focusing on viscous−elastic time scales which are typically significantly longer than elastic inertial time scales, we neglect solid's inertia and obtain the force balance between the fluidic, the elastic, the dielectric and the gravity forces

$$\tilde{F}_p + \tilde{k}(\tilde{h}_i - \tilde{h}(\tilde{t})) + \tilde{F}_d = \tilde{m}\tilde{g}. \tag{S23}$$

Substituting the expressions for $\tilde{F}_p$ and $\tilde{F}_d$, Eqs. (S21) and (S22), into Eq. (S23) yields the evolution equation for $\tilde{h}(\tilde{t})$

$$-\frac{\tilde{\mu}\tilde{l}_m^3}{\tilde{h}(\tilde{t})^3}\frac{\mathrm{d}\tilde{h}(\tilde{t})}{\mathrm{d}\tilde{t}} + \frac{6\tilde{\mu}\tilde{B}(\tilde{t})}{\tilde{h}(\tilde{t})^2} + \tilde{k}_g(\tilde{h}_i - \tilde{h}(\tilde{t})) + \frac{1}{2}\tilde{\varepsilon}\tilde{E}(\tilde{t})^2\tilde{l}_m = \tilde{m}\tilde{g}, \tag{S24}$$

where $\tilde{k}_g$ is the generalized spring stiffness consisting of contributions of linear elasticity and gravity

$$\tilde{k}_g = \tilde{k} + \left[1 + \frac{\tilde{l}_m + \tilde{l}_{sheet}}{4\tilde{l}_{res}}\right] \tilde{\rho}\tilde{g}\tilde{l}_m. \tag{S25}$$

The evolution equation (S24) is complemented by the initial condition,

$$\tilde{h}(\tilde{t}=0) = \tilde{h}_0, \tag{S26}$$

where $\tilde{h}_0 = \tilde{h}_i - (\tilde{m}\tilde{g}/\tilde{k}_g)$ is the initial liquid film thickness when the plate is at rest. For convenience, we express Eq. (S24) using the definition of $\tilde{h}_0$, and obtain an equation for the gap $\tilde{h}(\tilde{t})$ representing the force balance between the viscous resistance, the electro-osmotic and dielectric forces and the restoring effects of the elasticity and gravity

$$-\frac{\tilde{\mu}\tilde{l}_m^3}{\tilde{h}(\tilde{t})^3}\frac{\mathrm{d}\tilde{h}(\tilde{t})}{\mathrm{d}\tilde{t}} + \frac{6\tilde{\mu}\tilde{B}(\tilde{t})}{\tilde{h}(\tilde{t})^2} + \frac{1}{2}\tilde{\varepsilon}\tilde{E}(\tilde{t})^2\tilde{l}_m + \tilde{k}_g(\tilde{h}_0 - \tilde{h}(\tilde{t})) = 0. \tag{S27}$$

For the case of a constant applied voltage, $\tilde{B}$ is constant and thus Eq. (S27) reduces to

$$\frac{\tilde{\mu}\tilde{l}_m^3}{\tilde{h}(\tilde{t})^3}\frac{\mathrm{d}\tilde{h}(\tilde{t})}{\mathrm{d}\tilde{t}} = \frac{6\tilde{\mu}\tilde{B}}{\tilde{h}(\tilde{t})^2} + \frac{1}{2}\tilde{\varepsilon}\tilde{E}^2\tilde{l}_m + \tilde{k}_g(\tilde{h}_0 - \tilde{h}(\tilde{t})). \tag{S28}$$

For the case of a constant applied current, $\tilde{B}(\tilde{t})\tilde{h}(\tilde{t}) = \text{const} = \tilde{B}\tilde{h}_0$, and thus (S27) takes the form

$$\frac{\tilde{\mu}\tilde{l}_m^3}{\tilde{h}(\tilde{t})^3}\frac{\mathrm{d}\tilde{h}(\tilde{t})}{\mathrm{d}\tilde{t}} = \frac{6\tilde{\mu}\tilde{B}\tilde{h}_0}{\tilde{h}(\tilde{t})^3} + \frac{1}{2}\frac{\tilde{\varepsilon}\tilde{E}^2\tilde{l}_m\tilde{h}_0^2}{\tilde{h}(\tilde{t})^2} + \tilde{k}_g(\tilde{h}_0 - \tilde{h}(\tilde{t})), \tag{S29}$$

where $\tilde{B}$ denotes value of $\tilde{B}(\tilde{t})$ at $\tilde{t}=0$.

S.2.2. Normalizing the governing equations

Scaling by the characteristic dimensions, we define the following non-dimensional variables:

$$h = \frac{\tilde{h}}{\tilde{h}_0}, \quad x = \frac{\tilde{x}}{\tilde{l}_m}, \quad t = \frac{\tilde{t}}{\tilde{t}^*}, \tag{S30}$$

where $\tilde{t}^* = \tilde{\mu}\tilde{l}_m^3/\tilde{k}_g\tilde{h}_0^3$ is the viscous−elastic time scale obtained by balancing the first and the third terms in Eq. (S27).

Substituting Eq. (S30) into Eqs. (S28) and (S29), we obtain the non-dimensional evolution equations for the gap $h(t)$ **for the case of a constant applied voltage,**

$$\frac{1}{h^3}\frac{\mathrm{d}h}{\mathrm{d}t} = \frac{4}{27}\frac{\beta}{h^2} + \frac{4}{27}\varphi\beta^2 + 1 - h. \tag{S31a}$$

For the case of a constant applied current the equation takes the form

$$\frac{1}{h^3}\frac{\mathrm{d}h}{\mathrm{d}t} = \frac{4}{27}\frac{\beta}{h^3} + \frac{4}{27}\frac{\varphi\beta^2}{h^2} + 1 - h, \tag{S31b}$$

subject to the initial condition $h(t=0)=1$. In both cases, β defined as

$$\beta = \frac{81}{2}\frac{\tilde{B}}{\tilde{k}_g\tilde{h}_0^3/\tilde{\mu}} = \frac{81}{2}\lambda\frac{\tilde{\varepsilon}\tilde{\zeta}\tilde{E}\tilde{l}_m^2}{\tilde{k}_g\tilde{h}_0^3}, \tag{S32}$$

is a key governing non-dimensional parameter representing the ratio of electro-osmotic to elastic forces. An additional positive parameter φ, appearing in Eq. (S31), is defined as

$$\varphi = \frac{1}{486}\frac{\tilde{k}_g\tilde{h}_0^5}{\lambda^2\tilde{\varepsilon}\tilde{\zeta}^2\tilde{l}_m^3}, \tag{S33}$$

where λ is a non-dimensional parameter defined as

$$\lambda = \frac{\tilde{B}}{\tilde{\varepsilon}\tilde{\zeta}\tilde{E}\tilde{l}_m^2/\tilde{\mu}}. \tag{S34}$$

Initiating downward motion of the rigid plate requires a negative value of β, which together with the requirements $\mathrm{d}h/\mathrm{d}t < 0$ and $h = 1$ at $t = 0$, implies from Eq. (S31) that $1 + \varphi\beta > 0$. The physical range of β corresponding to descend of the rigid plate is thus

$$-\frac{1}{\varphi} < \beta < 0, \tag{S35}$$

and the transition from a downward to an upward motion of the plate occurs at $\beta = -1/\varphi$.

It is worth noting that while β changes by manipulation of the applied electric field, the parameters φ and λ remain constant for a given configuration. We also note that the product $\varphi\beta$ is a non-dimensional parameter representing the ratio of dielectric to electro-osmotic forces

$$\varphi\beta = \frac{1}{486}\frac{\tilde{k}_g\tilde{h}_0^5}{\lambda^2\tilde{\varepsilon}\tilde{\zeta}^2\tilde{l}_m^3} \times \frac{81}{2}\lambda\frac{\tilde{\varepsilon}\tilde{\zeta}\tilde{E}\tilde{l}_m^2}{\tilde{k}_g\tilde{h}_0^3} = \frac{1}{12}\frac{\tilde{E}\tilde{h}_0^2}{\lambda\tilde{\zeta}\tilde{l}_m}, \tag{S36}$$

which scales linearly with the applied electric field $\tilde{E}$.

S.3. LINEAR STABILITY ANALYSIS

We here perform linear stability analysis for constant voltage and constant current actuation modes. We consider a small perturbation of the rigid body from its equilibrium height h_{ss}, by letting $h(t) = h_{\mathrm{ss}}(1 + \epsilon_0 \mathrm{e}^{\sigma t})$, where $\epsilon_0 \ll 1$ is some small perturbation and σ is the non-dimensional growth rate. Substituting the perturbation into Eq. (S31), the leading order provides the equation for steady-state solution h_{ss}

$$O(1): \quad \frac{4}{27}\frac{\beta}{h_{\mathrm{ss}}^2} + \frac{4}{27}\varphi\beta^2 + 1 - h_{\mathrm{ss}} = 0 \quad \text{Constant voltage}, \tag{S37a}$$

$$O(1): \quad \frac{4}{27}\frac{\beta}{h_{\mathrm{ss}}^3} + \frac{4}{27}\frac{\varphi\beta^2}{h_{\mathrm{ss}}^2} + 1 - h_{\mathrm{ss}} = 0 \quad \text{Constant current}. \tag{S37b}$$

The first order, $O(\epsilon_0)$, yields the equation the growth rate of the perturbation σ

$$O(\epsilon_0): \quad \sigma = -\frac{8}{27}\beta - h_{\mathrm{ss}}^3 = h_{\mathrm{ss}}^2\left[2\left(1 + \frac{4}{27}\varphi\beta^2\right) - 3h_{\mathrm{ss}}\right] \quad \text{Constant voltage}, \tag{S38a}$$

$$O(\epsilon_0): \quad \sigma = -\frac{8}{27}\varphi\beta^2 - \frac{4}{9}\frac{\beta}{h_{\mathrm{ss}}} - h_{\mathrm{ss}}^3 = \frac{4}{27}\varphi\beta^2 + h_{\mathrm{ss}}^2(3 - 4h_{\mathrm{ss}}) \quad \text{Constant current}, \tag{S38b}$$

indicating that positive values of β, corresponding to positive (upward) deformation always result in a stable system, whereas negative values of β may destabilize it. It follows from Eq. (S38) that the critical steady-state height h_{ssCR}, below which the system is unstable, and the corresponding threshold value β_{CR} can be determined from the following nonlinear equations

$$h_{\mathrm{ssCR}} = \frac{2}{3}\left(1 + \frac{4}{27}\varphi\beta_{\mathrm{CR}}^2\right) \quad \text{and} \quad \beta_{\mathrm{CR}} + \left(1 + \frac{4}{27}\varphi\beta_{\mathrm{CR}}^2\right)^3 = 0 \quad \text{Constant voltage}, \tag{S39a}$$

$$h_{\mathrm{ssCR}} = \frac{3}{4} + \frac{1}{27}\frac{\varphi\beta_{\mathrm{CR}}^2}{h_{\mathrm{ssCR}}^2} \quad \text{and} \quad \beta_{\mathrm{CR}} + h_{\mathrm{ssCR}}\left(\frac{2}{3}\varphi\beta_{\mathrm{CR}}^2 + \frac{9}{4}h_{\mathrm{ssCR}}^3\right) = 0 \quad \text{Constant current}. \tag{S39b}$$

Figures S5(a) and S5(b) present the critical steady-state height h_{ssCR} and the corresponding threshold value β_{CR} as a function of φ for a constant voltage actuation mode, obtained from Eq. (S39a). We observe three different solution

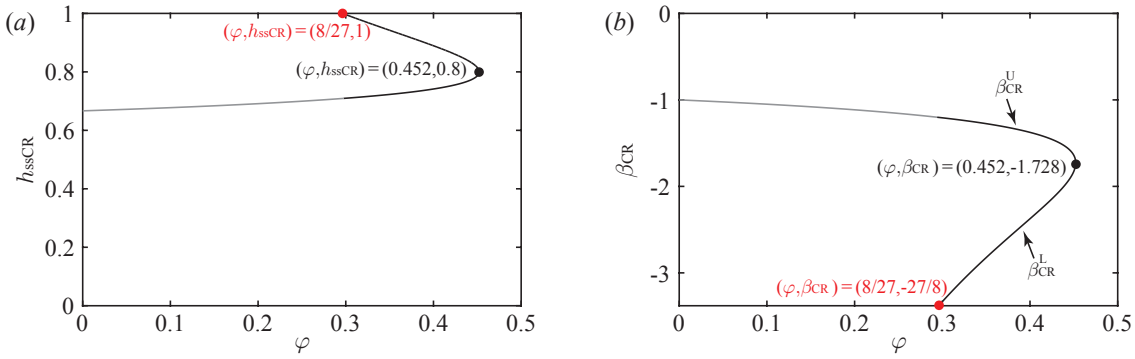

FIG. S5. Results of linear stability analysis for the case of a constant applied voltage. (a) The critical steady-state height $h_{\rm ssCR}$ and (b) the corresponding threshold value $\beta_{\rm CR}$ as a function of φ. For $0 \le \varphi < 8/27$, there is a single solution for $h_{\rm ssCR}$ and $\beta_{\rm CR}$, represented by gray lines. For $8/27 < \varphi < 0.452$, there are two solutions for $h_{\rm ssCR}$ and $\beta_{\rm CR} = (\beta^{\rm L}_{\rm CR}, \beta^{\rm U}_{\rm CR})$, represented by black lines, and the instability occurs within the range $|\beta^{\rm U}_{\rm CR}| < |\beta| < |\beta^{\rm L}_{\rm CR}|$. Above $\varphi = 0.452$, there is no physical solution for Eq. (S39a) and the system remains stable.

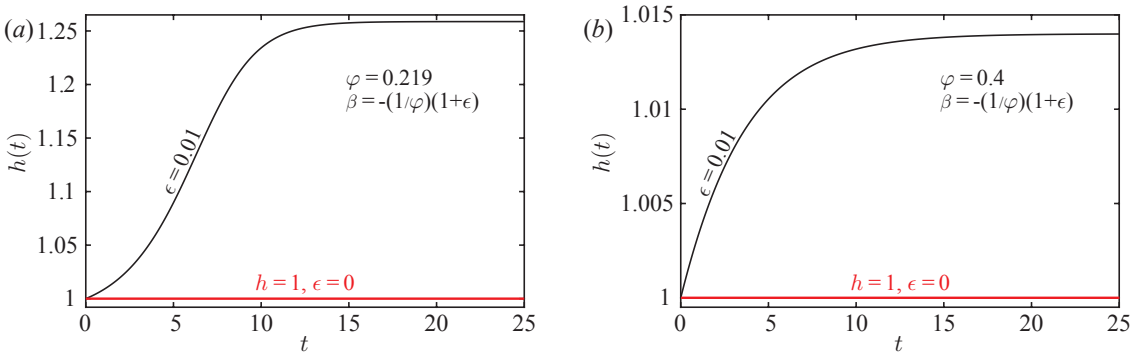

FIG. S6. The time evolution of the film thickness $h(t)$ for $\beta = -(1/\varphi)(1+\epsilon)$ and $\epsilon = 10^{-2}$ for (a) $\varphi = 0.219$ and (b) $\varphi = 0.4$. For $\varphi > 8/27$ the system is stable and a perturbation results in only a slight deviation from the initial location $h = 1$. For $\varphi < 8/27$, a perturbation from the initial state results in an initially unstable upward deformation, which is eventually balanced at sufficiently large deformations by the non-linear terms.

behaviors for $h_{\rm ssCR}$ and $\beta_{\rm CR}$ depending on the value of φ. (I) For $0 \le \varphi < 8/27$, there is a single solution for $h_{\rm ssCR}$ and $|\beta_{\rm CR}|$, which increases with φ. (II) For $8/27 < \varphi < 0.452$, there are two solutions for $h_{\rm ssCR}$ and $\beta_{\rm CR} = (\beta^{\rm L}_{\rm CR}, \beta^{\rm U}_{\rm CR})$ and the instability occurs within the range $|\beta^{\rm U}_{\rm CR}| < |\beta| < |\beta^{\rm L}_{\rm CR}|$, but for $|\beta| > |\beta^{\rm L}_{\rm CR}|$ the system transitions back to stable state. (III) Above $\varphi = 0.452$, there is no physical solution for Eq. (S39a) and the system always remains stable.

Using the results of the linear stability analysis, we can provide insight into the transition from a downward to an upward motion of the plate at $\beta = -1/\varphi$. Substituting $h_{\rm ss} = 1$ and $\beta = -1/\varphi$ into Eq. (S38a), yields the corresponding growth rate of the perturbation σ

$$\sigma = \frac{8}{27}\frac{1}{\varphi} - 1 \quad \text{for} \quad h_{\rm ss} = 1 \quad \text{and} \quad \beta = -1/\varphi, \quad \text{Constant voltage}, \tag{S40}$$

indicating that for $\varphi > 8/27$ the transition is from a stable upward motion to a stable downward motion, whereas for $\varphi < 8/27$ the transition is from a stable upward motion to an unstable downward motion.

Figure S6(a) presents the time evolution of the gap $h(t)$ for $\beta = -(1/\varphi)(1+\epsilon)$, with $\varphi = 0.219$ and a small perturbation $\epsilon = 10^{-2}$. A small change in the electric field leads to large changes in the deformation at short times, showing that the system is linearly unstable, consistent with Eq. (S38a). However, at longer times, the effect of nonlinear terms in Eq. (S31a) becomes apparent, and the plate reaches a steady state deformation. Figure S6(b) presents the time evolution of the gap $h(t)$ for $\beta = -(1/\varphi)(1+\epsilon)$, with $\varphi = 0.4$ and $\epsilon = 10^{-2}$, showing that for $\varphi > 8/27$ the upward deformation is a stable one and the system is only slightly perturbed from $h = 1$.

S.4. ESTIMATING MODEL PARAMETERS USING EXPERIMENTAL DATA

In this section, we estimate the values of the generalized spring stiffness $\tilde{k}_g$ and the parameter φ using physical and geometrical parameters from the experiments. Then, we use the obtained values to calculate the characteristic time scale $\tilde{t}^* = \tilde{\mu}\tilde{l}_m^3/\tilde{k}_g\tilde{h}_0^3$ and theoretically predict the threshold value of the applied electric field and the critical steady-state height.

Assuming a linear elastic response and using $\tilde{m} = 0.2\,\mathrm{gr}$, $\tilde{g} = 9.81\,\mathrm{m/s^2}$, $\tilde{h}_i = 117\,\mu\mathrm{m}$, $\tilde{h}_0 = 94\,\mu\mathrm{m}$ and $\tilde{w}_m = 10\,\mathrm{mm}$, we estimate the value of $\tilde{k}_g$ as

$$\tilde{k}_g = \frac{(\tilde{m}/\tilde{w}_m)\tilde{g}}{\tilde{h}_i - \tilde{h}_0} = \frac{(0.2\times 10^{-3}/10^{-2})\times 9.81}{(171-94)\times 10^{-6}} = 2548\,\mathrm{N/m^2}. \tag{S41}$$

Next, given a zeta potential value of $\tilde{\zeta} = -63\,\mathrm{mV}$ for glass [5], and assuming that the bottom surface of the chamber is patterned with regions of zeta potential that are equal in magnitude but opposite in sign [5], we obtain $\lambda = 0.25$. For $\tilde{l}_m = 10\,\mathrm{mm}$ and $\tilde{\varepsilon} = 7.08\cdot 10^{-10}\,\mathrm{F/m}$, we obtain an estimate for the parameter φ as

$$\varphi = \frac{1}{486}\frac{\tilde{k}_g\tilde{h}_0^5}{\lambda^2\tilde{\varepsilon}\tilde{\zeta}^2\tilde{l}_m^3} = 0.219. \tag{S42}$$

Using Eq. (S41) and taking $\tilde{\mu} = 10^{-3}\,\mathrm{Pa\,s}$, we estimate the characteristic time scale $\tilde{t}^*$ as

$$\tilde{t}^* = \frac{\tilde{\mu}\tilde{l}_m^3}{\tilde{k}_g\tilde{h}_0^3} = 0.473\ \mathrm{s}. \tag{S43}$$

Substituting the value of φ, given in Eq. (S42), into Eq. (S39a), yields

$$h_{\mathrm{ssCR}} = 0.694 \quad \text{and} \quad \beta_{\mathrm{CR}} = -1.129 \quad \text{for } \varphi = 0.219. \tag{S44}$$

Using the values of $\tilde{\zeta}$, $\tilde{k}_g$, $\tilde{h}_0$ and $\tilde{\varepsilon}$, it follows from Eqs. (S32) and (S44) that the theoretically predicted threshold value of the electric field is

$$\tilde{E}_{\mathrm{CR,Theory}} = \frac{2}{81}\frac{\beta_{\mathrm{CR}}}{\lambda}\frac{\tilde{k}_g\tilde{h}_0^3}{\tilde{\varepsilon}\tilde{\zeta}\tilde{l}_m^2} = -52927\,\mathrm{V/m}, \tag{S45}$$

which compares fairly well with the experimentally observed threshold value of the electric field

$$\tilde{E}_{\mathrm{CR,Exp}} = -22300\,\mathrm{V/m}. \tag{S46}$$

Given that the theoretical model is one-dimensional in space, we consider this to be a fairly good prediction (a factor of 2.5×, and certainly within the same order-of-magnitude). Other contributors to the quantitative difference may also be experimental uncertainties in the values of zeta potential and the parameter λ, and in the value of generalized spring stiffness $\tilde{k}_g$, which is estimated assuming a Hookian response of the elastic membrane.

S.5. DYNAMICS AFTER THE ONSET OF INSTABILITY AND COLLAPSE DURATION

In this section, we focus on a constant voltage actuation mode and examine the dynamics of the rigid body after the onset of instability in a bottleneck regime for electric field values near the threshold.

S.5.1. Analysis of the bottleneck phase

We here analyze the dynamics during the bottleneck phase. We follow Gomez *et al.* [7] and assume that the system is perturbed just beyond the threshold value β_{CR}, by setting

$$\beta = \beta_{\mathrm{CR}}(1+\delta), \tag{S47}$$

where $0 < \delta \ll 1$ is a normalized electric field difference, defined as

$$\delta = \frac{\tilde{E}}{\tilde{E}_{\mathrm{CR}}} - 1 = \frac{\beta}{\beta_{\mathrm{CR}}} - 1. \tag{S48}$$

During the bottleneck phase the height of the plate $h(t)$ is close to the value of h_{ssCR} , so we may write

$$h(t) = h_{\mathrm{ssCR}}(1 + H(t)), \tag{S49}$$

where $|H| \ll 1$. Substituting Eqs. (S47) and (S49) into Eq. (S31a) yields

$$\frac{\mathrm{d}H}{\mathrm{d}t} = \frac{4}{27}\beta_{\mathrm{CR}}(1+\delta)(1+H) + h_{\mathrm{ssCR}}^2(1+3H+3H^2+H^3)\left(\frac{4}{27}\varphi\beta_{\mathrm{CR}}^2(1+\delta)^2 + 1 - h_{\mathrm{ssCR}}(1+H)\right), \tag{S50}$$

which after some rearrangement leads to

$$\begin{aligned}\frac{\mathrm{d}H}{\mathrm{d}t} = &\left[\frac{4}{27}\beta_{\mathrm{CR}} + h_{\mathrm{ssCR}}^2(1-h_{\mathrm{ssCR}}) + \frac{4}{27}\varphi\beta_{\mathrm{CR}}^2 h_{\mathrm{ssCR}}^2\right] + H\left[\frac{4}{27}\beta_{\mathrm{CR}} + 3h_{\mathrm{ssCR}}^2 - 4h_{\mathrm{ssCR}}^3 + \frac{4}{9}\varphi\beta_{\mathrm{CR}}^2 h_{\mathrm{ssCR}}^2\right] \\ &+ \frac{4}{27}\beta_{\mathrm{CR}}\delta(1+2h_{\mathrm{ssCR}}^2\beta_{\mathrm{CR}}\varphi) + 3h_{\mathrm{ssCR}}^2\left(1 - 2h_{\mathrm{ssCR}} + \frac{4}{27}\varphi\beta_{\mathrm{CR}}^2\right)H^2 + O(\delta H, H^3).\end{aligned} \tag{S51}$$

It follows from Eqs. (S37a) and (S38a) that the first and the second brackets on the right-hand side of Eq. (S51) are zero and thus Eq. (S51) reduces to

$$\frac{\mathrm{d}H}{\mathrm{d}t} = \frac{4}{27}\beta_{\mathrm{CR}}\delta(1+2h_{\mathrm{ssCR}}^2\beta_{\mathrm{CR}}\varphi) + 3h_{\mathrm{ssCR}}^2\left(1 - 2h_{\mathrm{ssCR}} + \frac{4}{27}\varphi\beta_{\mathrm{CR}}^2\right)H^2 + O(\delta H, H^3). \tag{S52}$$

which is the normal form for overdamped dynamics near a saddle-node bifurcation [6]. We note that Eq. (S52) is valid provided the ordering $\delta \ll |H| \ll 1$, implying that the neglected terms of $O(\delta H, H^3)$ are smaller than the retained terms. The corresponding solution of Eq. (S52) is given by

$$H(t) = -\frac{2\sqrt{\delta}}{9h_{\mathrm{ssCR}}}\sqrt{\frac{\beta_{\mathrm{CR}}(1+2h_{\mathrm{ssCR}}^2\beta_{\mathrm{CR}}\varphi)}{1-2h_{\mathrm{ssCR}}+\frac{4}{27}\varphi\beta_{\mathrm{CR}}^2}}\tan\left[\frac{2}{3}h_{\mathrm{ssCR}}\sqrt{\delta}\sqrt{\beta_{\mathrm{CR}}(1+2h_{\mathrm{ssCR}}^2\beta_{\mathrm{CR}}\varphi)\left(1-2h_{\mathrm{ssCR}}+\frac{4}{27}\varphi\beta_{\mathrm{CR}}^2\right)}(t-t_0)\right], \tag{S53}$$

where t_0 is some constant. As noted by Gomez *et al.* [7], $H(t)$ grows with time and when it becomes $O(1)$, our original assumption $|H| \ll 1$ is no longer valid and the solution (S53) breaks down. This break down occurs since the tan function increases indefinitely as the term in square brackets approaches $\pm\pi/2$. Using the expansion $\tan x \sim \pm(\pi/2 \mp x)^{-1}$ as $x \to \pm\pi/2$, we obtain that the solution given by Eq. (S53) behaves as

$$H(t) \sim \mp\frac{9}{h_{\mathrm{ssCR}}^2|27-54h_{\mathrm{ssCR}}+4\beta_{\mathrm{CR}}^2\varphi|}\left(\frac{3\pi}{4h_{\mathrm{ssCR}}\sqrt{\delta\beta_{\mathrm{CR}}(1+2h_{\mathrm{ssCR}}^2\beta_{\mathrm{CR}}\varphi)(1-2h_{\mathrm{ssCR}}+\frac{4}{27}\beta_{\mathrm{CR}}^2\varphi)}} \mp (t-t_0)\right)^{-1}, \tag{S54}$$

implying that $H \sim O(1)$ when

$$t - t_0 \sim \pm\frac{3\pi}{4h_{\mathrm{ssCR}}\sqrt{\delta\beta_{\mathrm{CR}}(1+2h_{\mathrm{ssCR}}^2\beta_{\mathrm{CR}}\varphi)(1-2h_{\mathrm{ssCR}}+\frac{4}{27}\beta_{\mathrm{CR}}^2\varphi)}} + O(1). \tag{S55}$$

The bottleneck duration, denoted t_{BOT}, is simply the difference between these two values, so we obtain

$$t_{\mathrm{BOT}} = \frac{3\pi}{2h_{\mathrm{ssCR}}\sqrt{\delta\beta_{\mathrm{CR}}(1+2h_{\mathrm{ssCR}}^2\beta_{\mathrm{CR}}\varphi)(1-2h_{\mathrm{ssCR}}+\frac{4}{27}\beta_{\mathrm{CR}}^2\varphi)}} + O(1). \tag{S56}$$

Because the solution for $H(t)$ is antisymmetric about t_0, it follows that t_0 is simply half of the bottleneck duration

$$t_0 \sim \frac{3\pi}{4h_{\mathrm{ssCR}}\sqrt{\delta\beta_{\mathrm{CR}}(1+2h_{\mathrm{ssCR}}^2\beta_{\mathrm{CR}}\varphi)(1-2h_{\mathrm{ssCR}}+\frac{4}{27}\beta_{\mathrm{CR}}^2\varphi)}} + O(1). \tag{S57}$$

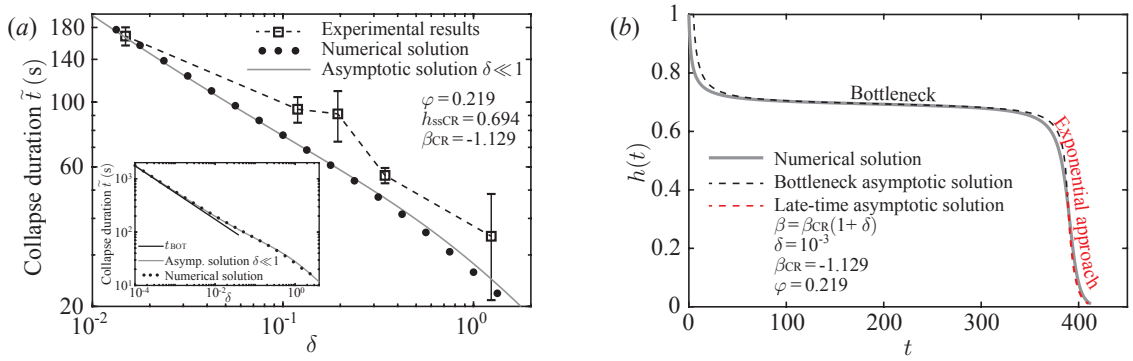

FIG. S7. Investigation of dynamics and collapse duration after the onset of instability. (a) Collapse duration as a function of δ, corresponding to the time required for the system to reach 1% of its initial height after the onset of instability. Black squares and dots represent experimental and numerical results, respectively. Error bars indicate a 95% confidence on the mean based on four experiments. To present the non-dimensional theoretical results in dimensional form we scale them by $\tilde{t}^* = 1.3995\,\mathrm{s}$ obtained by fitting the model to a single experimental data point at $\delta = 1.49 \times 10^{-2}$, $\tilde{t} = 168.2\,\mathrm{s}$. The gray line represents the asymptotic solution (S64) for $\delta \ll 1$. Inset: Theoretically predicted collapse duration for a wide range of δ values. Black dots represents the numerical results. The black line represents the prediction (S56) based on the bottleneck time alone in the limit $\delta \ll 1$, and the gray line represents the solution (S64) accounting also for the late time asymptotic behavior. (b) Comparison between asymptotic and numerical solutions for the time evolution of the gap $h(t)$, with $\delta = 10^{-3}$ and $\varphi = 0.219$. Black and red dashed lines represent asymptotic predictions (S59) and (S61) for $\delta \ll 1$, whereas gray line represents the numerical solution.

Finally, combining Eqs. (S49), (S53) and (S57) provides the explicit expressions for $H(t)$ and $h(t)$ in the bottleneck phase

$$H(t) \sim -\frac{2\sqrt{\delta}}{9h_{\mathrm{ssCR}}}\sqrt{\frac{\beta_{\mathrm{CR}}(1+2h_{\mathrm{ssCR}}^2\beta_{\mathrm{CR}}\varphi)}{1-2h_{\mathrm{ssCR}}+\frac{4}{27}\varphi\beta_{\mathrm{CR}}^2}}\tan\left[\frac{2}{3}h_{\mathrm{ssCR}}\sqrt{\delta}\sqrt{\beta_{\mathrm{CR}}(1+2h_{\mathrm{ssCR}}^2\beta_{\mathrm{CR}}\varphi)\left(1-2h_{\mathrm{ssCR}}+\frac{4}{27}\varphi\beta_{\mathrm{CR}}^2\right)}t-\frac{\pi}{2}\right], \tag{S58}$$

and

$$h(t) \sim h_{\mathrm{ssCR}}-\frac{2}{9}\sqrt{\delta}\sqrt{\frac{\beta_{\mathrm{CR}}(1+2h_{\mathrm{ssCR}}^2\beta_{\mathrm{CR}}\varphi)}{1-2h_{\mathrm{ssCR}}+\frac{4}{27}\varphi\beta_{\mathrm{CR}}^2}}\tan\left[\frac{2}{3}h_{\mathrm{ssCR}}\sqrt{\delta}\sqrt{\beta_{\mathrm{CR}}(1+2h_{\mathrm{ssCR}}^2\beta_{\mathrm{CR}}\varphi)\left(1-2h_{\mathrm{ssCR}}+\frac{4}{27}\varphi\beta_{\mathrm{CR}}^2\right)}t-\frac{\pi}{2}\right]. \tag{S59}$$

S.5.2. Late-time behavior for $\delta \ll 1$

To determine the collapse duration in the limit of $\delta \ll 1$, we need to account for the late-time behavior. In the late-time period, $h \ll 1$ and $t \gg 1$, the electro-osmotic force balances the viscous resistance while the elastic and dielectric forces are negligible. Therefore, it follows from Eq. (S31a)

$$\frac{\mathrm{d}h}{\mathrm{d}t} \sim \frac{4}{27}\beta_{\mathrm{CR}}(1+\delta)h \quad \text{as} \quad h \ll 1, \tag{S60}$$

which after integration yields

$$h(t) \sim h_{\mathrm{LT}} \exp\left[\frac{4}{27}\beta_{\mathrm{CR}}\,(1+\delta)\,(t-t_{\mathrm{LT}})\right], \tag{S61}$$

where h_{LT} and t_{LT} are the corresponding height and time, respectively, where this solution starts to be valid.

For $\delta \ll 1$, we determine h_{LT} and t_{LT} by matching the late-time asymptotic solution (S61) to the bottleneck solution (S59). Requiring that the solutions and their time-derivatives are equal at $h_{\mathrm{LT}}(t_{\mathrm{LT}})$, we find

$$h_{\mathrm{LT}} = h_{\mathrm{ssCR}} + \frac{2}{81}\frac{\beta_{\mathrm{CR}}(1+\delta)+\sqrt{\beta_{\mathrm{CR}}\left(\beta_{\mathrm{CR}}(1+\delta)^2+81h_{\mathrm{ssCR}}^2\left(1-2h_{\mathrm{ssCR}}+\frac{4}{27}\varphi\beta_{\mathrm{CR}}^2\right)\left(1-2h_{\mathrm{ssCR}}^2\beta_{\mathrm{CR}}\varphi\delta\right)\right)}}{h_{\mathrm{ssCR}}\left(1-2h_{\mathrm{ssCR}}+\frac{4}{27}\varphi\beta_{\mathrm{CR}}^2\right)}, \tag{S62}$$

and

$$t_{\rm LT}=\frac{3}{2h_{\rm ssCR}}\frac{1}{\sqrt{\delta}}\frac{1}{\sqrt{\beta_{\rm CR}(1+2h_{\rm ssCR}^2\beta_{\rm CR}\varphi)\left(1-2h_{\rm ssCR}+\frac{4}{27}\varphi\beta_{\rm CR}^2\right)}}\left[\tan^{-1}\left[\frac{h_{\rm ssCR}-h_{\rm LT}}{\frac{2}{9}\sqrt{\delta}}\sqrt{\frac{1-2h_{\rm ssCR}+\frac{4}{27}\varphi\beta_{\rm CR}^2}{\beta_{\rm CR}(1+2h_{\rm ssCR}^2\beta_{\rm CR}\varphi)}}\right]+\frac{\pi}{2}\right]. \tag{S63}$$

Since the rigid body approaches the bottom surface exponentially, in order to estimate the late-time duration we take $h_f=10^{-2}$ as the final height, and thus from Eq. (S61) we obtain the approximate expression for the collapse duration

$$t_{\rm TOT}=t_{\rm LT}+\frac{27}{4\beta_{\rm CR}(1+\delta)}\ln\frac{h_f}{h_{\rm LT}}\quad\text{for}\quad\delta\ll1, \tag{S64}$$

Figure S7(a) compares the experimentally (squares) and theoretically predicted (dots and gray line) collapse duration as a function of δ, with $\varphi=0.219$. While our theoretical model does not account for various effects, such as three-dimensionality and nonlinear elastic effects, the model captures well the monotonic decrease of the collapse duration observed in the experiments. Figure S7(a) (inset) presents the theoretically predicted collapse duration for a wide range of δ values. For very small values of δ, the total collapse time is dominated by the bottleneck time $t_{\rm BOT}$ (i.e. the initial and final transients are very short in comparison), which scales as $\delta^{-1/2}$ (see Eq. (S56)) and is presented by the black line. This time scale is similar to the one obtained in overdamped MEMS devices [7]. Significant improvement in the analytically predicted collapse time can be obtained by accounting for the late time asymptotic behavior in the limit $\delta\ll1$, as given in Eq. (S64) and provided by the gray line. Surprisingly, the approximation captures well the collapse time even for large values of δ and exhibits a change in slope consistent with the numerical results.

In Fig. S7(b) we compare the asymptotic (black and red dashed lines) and numerical (gray solid line) solutions for the time evolution of the gap $h(t)$, with $\delta=10^{-3}$ and $\varphi=0.219$. It is evident that the asymptotic results corresponding to Eq. (S59) for $t<t_{\rm LT}$ (black dashed line) and Eq. (S61) for $t_{\rm LT}<t<t_{\rm TOT}$ (red dashed line) are in good agreement with the numerical solution.

[1] R. Barnkob, C. J. Kahler, and M. Rossi, Lab Chip **15**, 3556 (2015).
[2] L. G. Leal, *Advanced Transport Phenomena: Fluid Mechanics and Convective Transport Processes* (Cambridge University Press, Cambridge, 2007).
[3] R. J. Hunter, *Foundations of Colloid Science* (Oxford University Press, New York, 2001).
[4] L. D. Landau and E. M. Lifshitz, *Electrodynamics of Continuous Media* (Pergamon Press, Bristol, 1960).
[5] F. Paratore, E. Boyko, G. V. Kaigala, and M. Bercovici, Phys. Rev. Lett. **122**, 224502 (2019).
[6] S. H. Strogatz, *Nonlinear Dynamics and Chaos: With Applications to Physics, Chemistry and Engineering* (Addison-Wesley, Reading, MA, 1994).
[7] M. Gomez, D. E. Moulton, and D. Vella, J. Micromech. Microeng. **28**, 015006 (2017).